Solar RRL
www.solar-rrl.com

Pathways toward 30% Efficient Single-Junction Perovskite Solar Cells and the Role of Mobile Ions

*Jonas Diekmann, Pietro Caprioglio, Moritz H. Futscher, Vincent M. Le Corre, Sebastian Reichert, Frank Jaiser, Malavika Arvind, Lorena Perdigón Toro, Emilio Gutierrez-Partida, Francisco Peña-Camargo, Carsten Deibel, Bruno Ehrler, Thomas Unold, Thomas Kirchartz, Dieter Neher, and Martin Stolterfoht**

Perovskite semiconductors have demonstrated outstanding external luminescence quantum yields, enabling high power conversion efficiencies (PCEs). However, the precise conditions to advance to an efficiency regime above monocrystalline silicon cells are not well understood. Herein, a simulation model that describes efficient p–i–n-type perovskite solar cells well and a range of different experiments is established. Then, important device and material parameters are studied and it is found that an efficiency regime of 30% can be unlocked by optimizing the built-in voltage across the perovskite layer using either highly doped (10^{19} cm^{-3}) transport layers (TLs), doped interlayers or ultrathin self-assembled monolayers. Importantly, only parameters that have been reported in recent literature are considered, that is, a bulk lifetime of 10 µs, interfacial recombination velocities of 10 cm s^{-1}, a perovskite bandgap (E_{gap}) of 1.5 eV, and an external quantum efficiency (EQE) of 95%. A maximum efficiency of 31% is predicted for a bandgap of 1.4 eV. Finally, it is demonstrated that the relatively high mobile ion density does not represent a significant barrier to reach this efficiency regime. The results of this study suggest continuous PCE improvements until perovskites may become the most efficient single-junction solar cell technology in the near future.

1. Introduction

Over the last 10 years perovskite solar cells have triggered an enormous research interest and with PCEs of 25.5%[1] they are close to the efficiencies of monocrystalline silicon solar cells (26.7%).[2,3] As such, perovskites provide an exciting opportunity to approach the thermodynamic efficiency limit of single-junction perovskite solar cells (33.7%[4,5]) due to their exceptional optical and material properties. An optimal semiconductor for solar cell applications must basically fulfil three requirements, that is, 1) a high absorption coefficient, in particular strong absorption at the band edge, 2) long charge carrier diffusion lengths to efficiently collect charges in several hundred nanometer thick films, and 3) a high photoluminescence quantum yield (PLQY).[6] Despite the impressive efficiencies achieved with perovskite solar cells, there are many other key considerations that need to be addressed prior to a successful commercialization of the technology. This includes the operational device stability, which may degrade when

J. Diekmann, Dr. P. Caprioglio, Dr. V. M. Le Corre, Dr. F. Jaiser, Dr. M. Arvind, L. P. Toro, E. Gutierrez-Partida, F. Peña-Camargo, Prof. D. Neher, Dr. M. Stolterfoht
Institute of Physics and Astronomy
University of Potsdam
Karl-Liebknecht-Str. 24-25, 14476 Potsdam-Golm, Germany
E-mail: stolterf@uni-potsdam.de

Dr. M. H. Futscher, Prof. B. Ehrler
AMOLF
Center for Nanophotonics
Science Park 104, 1098 XG Amsterdam, The Netherlands

The ORCID identification number(s) for the author(s) of this article can be found under https://doi.org/10.1002/solr.202100219.

DOI: 10.1002/solr.202100219

S. Reichert, Prof. C. Deibel
Institut für Physik
Technische Universität Chemnitz
09126 Chemnitz, Germany

Dr. T. Unold
Department of Structure and Dynamics of Energy Materials
Helmholtz-Zentrum-Berlin
Hahn-Meitner-Platz 1, 14109 Berlin, Germany

Prof. T. Kirchartz
IEK5-Photovoltaik
Forschungszentrum Jülich GmbH
52425 Jülich, Germany

subjected to illumination, oxygen,[7] heat,[8] or moisture.[9] Lead-based perovskites also raise concerns due to the possible pollution caused by this toxic heavy metal.[10] Furthermore, commercialization of perovskite solar cells requires a massive upscaling of production, which requires a suitable fabrication process that ensures good performance and a high level of reliability.[11] Notwithstanding these points, to improve the efficiencies of state-of-the-art perovskite cells further it is imperative to suppress all nonradiative recombination to an absolute minimum. This is particularly the case for the perovskite/transport layer (TL) interfaces but also for the perovskite absorber itself. This task requires a deep understanding of defect chemistry and device physics. Very encouraging in this regard are recent studies that highlighted exceptional external photoluminescence (PL) efficiencies (PLQY) in several perovskite compositions.[12–17] For example, Braly et al.[13] demonstrated an external fluorescence yield of 20% with a charge carrier bulk lifetime (τ_{bulk}) of ≈8.8 μs, even with the most standard methyl ammonium lead iodide (MAPI) perovskite absorber, which was passivated with trioctylphosphine oxide (TOPO).[18,19] Even higher PLQYs were demonstrated on a neat, potassium-passivated mixed perovskite film; however, no lifetimes were specified.[12] It is also clear that when it comes to complete cells, a key consideration is the nonradiative loss at the interfaces. A suitable approach to quantify the nonradiative recombination loss at the interface is based on absolute PL.[20–22] In fact, many recent record cells now commonly report luminescence quantum efficiencies of several percent, which underlines the exceptional optoelectronic quality of the whole device stack.[15] Important parameters that define the nonradiative interfacial recombination loss are the interface recombination velocity (S) and the energy offsets between the TLs and the perovskite.[23,24] Both parameters depend on the underlying substrate and the specific chemical environment at the interface.[25] In very high-efficiency systems, S can be reduced to be of the order of 10 cm s^{-1},[14,24,26] although this parameter is not routinely quantified in the literature and further research must be done to clearly disentangle the interfacial charge transfer and recombination based on kinetic measurements, such as transient PL.[22,24,26–29]

A key consideration to improve the efficiency of single junction cells is to lower the bandgap (E_{gap}) to the optimum value in the Shockley–Queisser model (e.g., ≈1.34 eV).[4,5] Commonly used perovskites such as methylammonium lead iodide (MAPI)[30,31] and formamidinium lead iodide (FAPI)[32–34] do allow some flexibility in modifying the bandgap within a range of 1.6 to ≈1.5 eV,[35] while $CsPbBr_3$ allows us to increase the bandgap further to 2.4 eV,[36] which is an important consideration for tandem solar cell applications.[23] Notably, both MAPI and FAPI perovskite cells allow achieving PCEs above 20%.[22,31,37] Moreover, the incorporation of small amounts of Sn[38–40] allows reducing the bandgap to the optimum bandgap in the Shockley-Queisser (SQ) model (1.1–1.4 eV) and PCEs above 21% have been reported for cells based on a 1.22 eV perovskite bandgap in 2019.[41] Unfortunately, tin perovskite brings other problems due to the high probability of oxidation from Sn^{2+} to Sn^{4+}.[40] Other key parameters include the donor and acceptor density (n_{dop}) in the TLs (i.e., doping),[42–44] the charge carrier mobilities (μ) in all layers,[45] and the kinetics and density of mobile ions (n_{ions}), which are expected to screen and redistribute the internal field, thereby causing recombination losses and hysteresis effects.[37,46–49] Other important considerations include the built-in voltage (V_{BI}) across the device and the energy-level alignment between the perovskite and the charge TLs for majority carriers (ΔE_{maj}).[50–52] It is fair to say that until today the impact of most of these parameters remains heavily debated in the community and there exist many conflicting findings in the literature with regard to these parameters. For example, so far, no consensus has been reached on the density of mobile ions with reported values typically varying from 10^{15} to 10^{19} cm^{-3} for MAPI.[48,53–55] Moreover, some literature reports suggest that the energy-level alignment does not play an important role for the device performance,[56] which is in contrast to other studies where the V_{OC} correlated to ΔE_{maj}.[27,57–59] Also, the distribution of the built-in potential across the device remains in general poorly understood despite significant progress in this regard.[37,60–62] Other examples include the chemical doping, with several reports linking doping to enhanced losses in V_{OC} or quasi-Fermi-level splitting (QFLS),[63–65] although in many inorganic solar cell technologies doping is a key factor in preventing minority carrier recombination at the metal contacts.[3,66]

In this work, we aim to understand the most promising and simple optimization strategies to allow perovskites to reach and surpass the efficiency of monocrystalline silicon and even GaAs (29.1%).[1] To this end we have optimized previously validated device simulations based on the well-established drift-diffusion simulator SCAPS,[67,68] by fitting the simulations to a number of different experimental results. Furthermore, the numerical simulations were extended to incorporate mobile ions based on experimentally measured diffusion constants and ion densities using the software IonMonger.[69,70] Based on a set of standard simulation parameters that describe a typical p–i–n-type cell (with a PCE of 19.2%), we have varied several important parameters to understand their relative importance within the limits of the simulation model, such as n_{dop}, n_{ions}, V_{BI}, E_{maj}, E_{gap}, S, τ_{bulk}, and the device absorption. Starting from the standard simulation, we find that increasing the carrier mobilities (in all layers) by a factor of 10 may only lead to small efficiency improvements (≈1% absolute) by allowing fill factors (FFs) of up to 85%. This is in contrast to electronic doping of the transport layers ($n_{dop} = 10^{19}$ cm^{-3}) which allows exceeding FFs of 85% and to reach V_{OC} close to the radiative limits with PCEs of 24% for the standard cell configuration. We explain the potentially huge benefit of doped TLs through an effective increase of the V_{BI} across the absorber layer, which repels minority carriers from the interfaces, thereby reducing interfacial recombination losses. Related to this, we show that a high dielectric constant in the neat material would lead to a decrease in FF due to a decrease in the V_{BI} across the absorber layer. These considerations imply the importance of maximizing the V_{BI} across the perovskite and also imply the benefit of a small ion density to prevent a screening of the internal field ($n_{ion} \ll$ electrode charge/volume ≈10^{16} cm^{-3}). Nevertheless, the experimentally measured mobile ion density greatly exceeds this critical value (≥6×10^{16} cm^{-3}) and we discuss the implication of this on the device performance. Finally, we demonstrate that 30% efficient perovskite solar cells are within reach by only using parameters that have already been demonstrated in the recent literature, i.e., a bandgap of ≈1.5 eV, a

bulk carrier lifetime of 10 μs, an interfacial recombination velocity of 10 cm s^{-1}, and an external quantum efficiency (EQE) of 95% throughout the spectrum. The key to unlock this efficiency regime is to maximize the device built-in field by either increasing the doping concentration in the TLs to at least 10^{19} cm^{-3} or using ultrathin (≈10 nm), undoped TLs, if a strong built-in field can be created by other means. Finally, we show that although the mobile ion density is very significant in our triple-cation perovskite devices ($\geq 6 \times 10^{16}$ cm^{-3}), it will most likely not represent a significant barrier for reaching such near-ideal solar cell performances as the relative impact of the mobile ions decreases with reduced interfacial and bulk recombination.

2. Results

In the first part of the study, we optimized our SCAPS[67,68] device simulation parameters by fitting several experimental results. First, standard simulation parameters were established to describe our reference cells with the following architecture: ITO/PTAA/PFN-Br/perovskite/C_{60}/BCP/Cu, where ITO is indium tin oxide, PTAA is poly[bis(4-phenyl)(2,4,6-trimethylphenyl)amine], PFN-Br is Poly({9,9-bis[30-({*N*,*N*-dimethyl}-*N*-ethylammonium)-propyl]-2,7-fluorene}-alt-2,7-{9,9-di-*n*-octylfluorene}) dibromide, and BCP is bathocuproine.[22,71] These cells exhibit on average a V_{OC} of ≈1.13 V, a FF of 79%, and a short-circuit current density of 21.5 mA cm^{-2} with an average EQE of close to 88% between 400 and 750 nm (Figure S1, Supporting Information), which results in a PCE of ≈19.2%.[22] We note these p–i–n-type cells initially exhibit essentially no hysteresis at different scan speeds that are accessible with our standard *JV*-measurement setup (scan rate <150 mV s^{-1}, Figure S2, Supporting Information), which, however, does not imply the absence of a hysteresis at even faster scan speeds. Using transient PL (TRPL) measurements, we obtained an interface recombination velocity of $S = 2000$ cm s^{-1} at the perovskite/electron transport layer (ETL) interface and $S = 100$ cm s^{-1} at the hole transport layer (HTL)/perovskite interface, as well as a bulk lifetime τ_{bulk} of 500 ns (Figure S3, Supporting Information).[22] Moreover, we note that the perovskite layer is effectively undoped (≈6×10^{11} cm^{-3}) as evidenced by lateral conductivity measurements (Figure S4, Supporting Information). A fit of the standard simulations to experimental *JV* curves is shown in a linear representation in **Figure 1**a, while Figure 1b shows a fit to the dark *JV* characteristic in a logarithmic representation. This demonstrates that the total recombination current in the cell is well described. We note a shunt resistance of 2.5×10^6 Ω cm^{-2} was used to describe the shunt regime at lower voltages (<0.7 V). All simulation parameters are shown in Table S1, Supporting Information. The set of basic equations solved by SCAPS is presented in Supporting Note S1, Supporting Information. Importantly, we used a bandgap-dependent bimolecular recombination coefficient (k_2) as detailed in Supporting Note S2, Supporting Information. Knowing the radiative recombination current density in the dark and the effective density of states $N_C = N_V = 2.2 \times 10^{18}$ cm^{-3},[26] k_2 can be readily obtained (e.g., for a bandgap of 1.63 eV, we obtain $k_2 = 3 \times 10^{-11}$ cm^3 s^{-1}).[72,73] We note that this represents the external k_2, which is impacted by photon recycling inside the bulk.[6,74–77] Therefore, by using the external k_2, we effectively consider the effect of photon recycling in our simulations. Importantly, using the bandgap-dependent k_2 and no parasitic losses, we can well reproduce the Shockley–Queisser efficiency versus bandgap (Figure S5, Supporting Information) with a maximum PCE of 33.77% at a bandgap of 1.36 eV.[5] Note, the precise value of k_2 has no impact under a 1 sun illumination for cells that are limited by Shockley-Read-Hall (SRH) recombination in the bulk or at the interfaces (such as the standard cell). Moreover, it is interesting to note that the reported Auger recombination coefficients (10^{-28} cm^{-6} s^{-1})[72] reduce the maximum obtainable PCE in our simulations by only 0.03% and are therefore not a limiting factor. The simulated parallel recombination currents in the perovskite layer, interface, and/or metal contacts are shown in Figure 1c, which accurately correspond to the experimentally obtained recombination currents (Figure 1d). The latter were obtained by measuring the QFLS of individual perovskite/transport layer films of the cell as reported in a previous publication.[50] Notably, at V_{OC}, interfacial recombination outweighs the recombination in the neat material by more than one order of magnitude. Moreover, the simulations reproduce the ideality factor of the standard cells of ≈1.35 across a broad range of light intensities (Figure 1e).[78] Based on these settings, several recent experimental results were fitted by changing only one parameter depending on the particular experiment. These experiments include cells with reduced interface recombination at the perovskite/ETL interface upon adding LiF (Figure 1f),[22] cells with different HTLs resulting in different V_{OC} (Figure 1g),[50] as well as cells with different PTAA layer thicknesses resulting in different FFs (Figure 1h).[45,79] Overall, Figure 1 shows that the SCAPS simulations can well reproduce these experimental results while also producing the quantified recombination currents in the bulk and the interfaces by taking into account the measured interface and bulk lifetimes.

2.1. Mobile Ions

Despite the good fits shown in Figure 1, it is important to note that the aforementioned SCAPS simulations were performed assuming a negligible mobile ion density.[43–46] To address the role of mobile ions on our simulation results, we performed additional experiments and simulations using the open-source simulation software IonMonger.[59,60] In a first step, we confirmed the comparability of IonMonger and SCAPS (without mobile ions) by comparing the key parameters such as *S* and the majority carrier offset E_{maj} (Figure S6, Supporting Information), which provided very similar results. To implement the mobile ion density in IonMonger, we first quantified the ion diffusion constant and activation energy (E_A) using transient capacitance measurements following a recently introduced approach (Figure S7, Supporting Information).[48,53,80] We note that we observed in fact the features of two mobile ion species; however, for simplicity we only considered the faster component in the simulations ($D_{ion} = 6 \times 10^{-10}$ cm^2 s^{-1} and $E_A = 120$ meV). Moreover, to estimate the ion density in our cells, we used bias-assisted charge extraction (BACE) experiments (Figure S8, Supporting Information). The BACE measurements indicate an ion density of 6×10^{16} cm^{-3} at a collection voltage of −1.6 V, which is consistent with Bertulozzi et al., who obtained a value of 7×10^{16} cm^{-3}

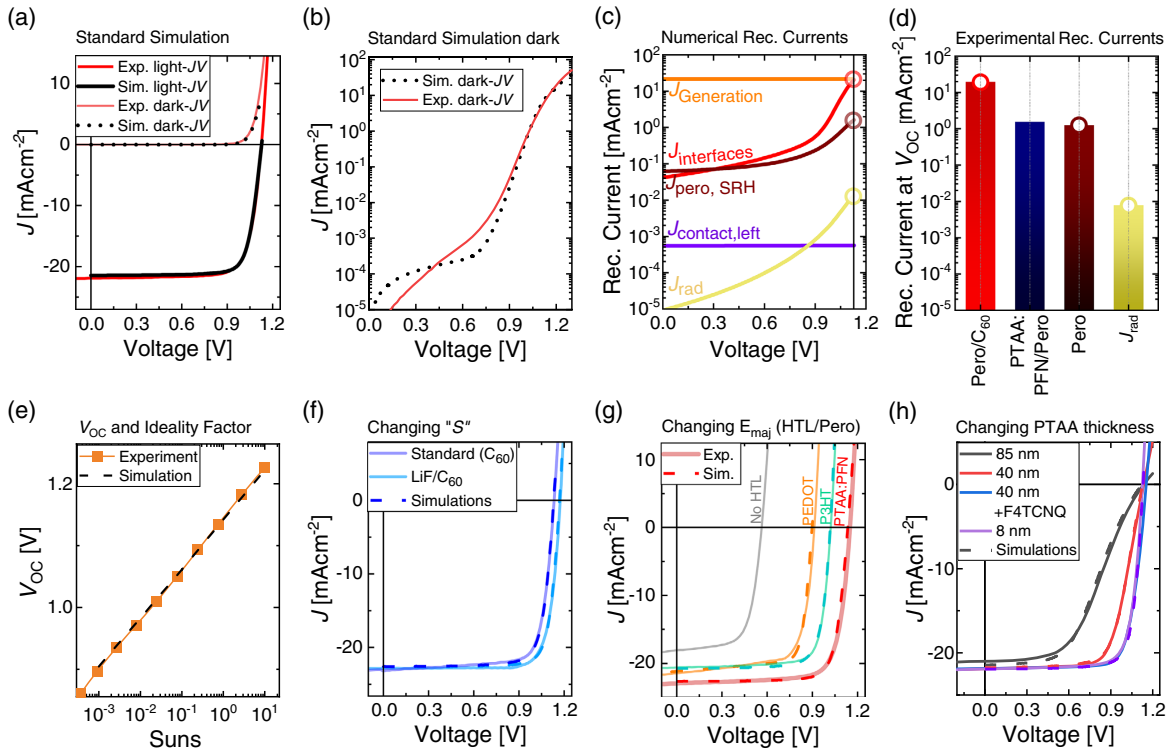

Figure 1. a,b) Experimental and numerically simulated light and dark *JV* curves of p–i–n-type cells based on PTAA/PFN-Br/triple-cation perovskite/C_{60} in a linear and logarithmic representation. The interface recombination velocities and bulk lifetime were obtained from TRPL measurements.[22] c) Simulated voltage-dependent radiative and nonradiative recombination currents in the neat perovskite and at both interfaces compared to the generation current. Interfacial recombination reduces the possible open-circuit voltage, which is roughly 10× larger than Shockley–Read–Hall recombination in the neat material. d) This is consistent with experimentally measured recombination currents under open-circuit conditions using steady-state PL measurements.[50] e) The simulation parameter set also reproduces the ideality factor ($n_{ID} \approx 1.35$) of the standard cells.[78] The standard simulation settings allow us to fit several experimental results by changing a single parameter depending on the particular experiment. f) Inserting LiF between the perovskite and C_{60} leads to concurrent increase of the TRPL lifetime, device V_{OC}, and PCEs above 21%.[22] The TRPL results suggest that *S* decreases by one order of magnitude upon application of LiF, which allows us to reproduce the experimentally observed V_{OC} gain of 35 mV. g) Cells with different HTLs and varying majority carrier band offsets as obtained from ultraviolet photoelectron spectroscopy (UPS) measurements.[50] Implementing energy offsets at the p-interface for the cells with a poly(3,4-ethylenedioxythiophene) polystyrene sulfonate (PEDOT:PSS) and poly(3-hexylthiophen-2,5-diyl) (P3HT) hole transport layer allows us to reproduce the experimental *JV* curves. h) Cells with changing PTAA thickness. The mobility in the PTAA layer has a significant impact on the device FF consistent with previous work.[79] The fitting allowed us to fine-tune the perovskite and the PTAA layer mobility ($\mu_{pero} = 1\ cm^2\ V^{-1}\ s^{-1}$, $\mu_{PTAA} = 1.5 \times 10^{-4}\ cm^2\ V^{-1}\ s^{-1}$, while $\mu_{C60} = 1.0 \times 10^{-2}\ cm^2\ V^{-1}\ s^{-1}$).

for double-cation/halide perovskite compositions (e.g., $Cs_{0.17}FA_{0.83}Pb(I_{0.83}Br_{0.17})_3$). Unfortunately, as larger collection voltages would break the devices, we can presently not exclude that the ion density is larger than the obtained value. **Figure 2**a,b displays the obtained V_{BI} distribution in steady state from IonMonger upon implementing a mobile ion density of $6 \times 10^{16}\ cm^{-3}$ (assumed to be halide vacancies), in comparison to the idealized homogenous distribution obtained in SCAPS. Figure 2c–e shows a good agreement between both simulation programs in terms of the *JV* scan, bulk and interface recombination currents, as well as ideality factor. We note that we used similar simulation parameters for both programs; however, to compensate for the detrimental effect of the significant ion density in IonMonger, we used a slightly higher built-in voltage (+100 mV). Overall, this comparison shows that both programs provide very similar results and although the mobile ion density significantly redistributes the V_{BI}, its effect on the device performance is rather small (i.e., ≈1.5% in PCE), which is obtained by comparing the PCE in case with and without mobile ions in IonMonger.

Starting from this simulation set, we aim to find the most promising ways to improve the PCE of perovskite solar cells. A large set of simulations was performed to check most parameters accessible in SCAPS and IonMonger. We note that in the following, we will show the results as obtained from SCAPS, while IonMonger simulations are shown again toward the end of the study. We also emphasize that we have cross-checked each simulation with IonMonger including the measured ion concentration, which led to very similar results and identical trends.

2.2. Mobility and TL Doping

A generic approach to optimize the performance of a solar cell is to maximize the carrier mobility to improve the charge-extraction efficiency. To this end, we first varied the majority carrier mobility in the HTL and ETL

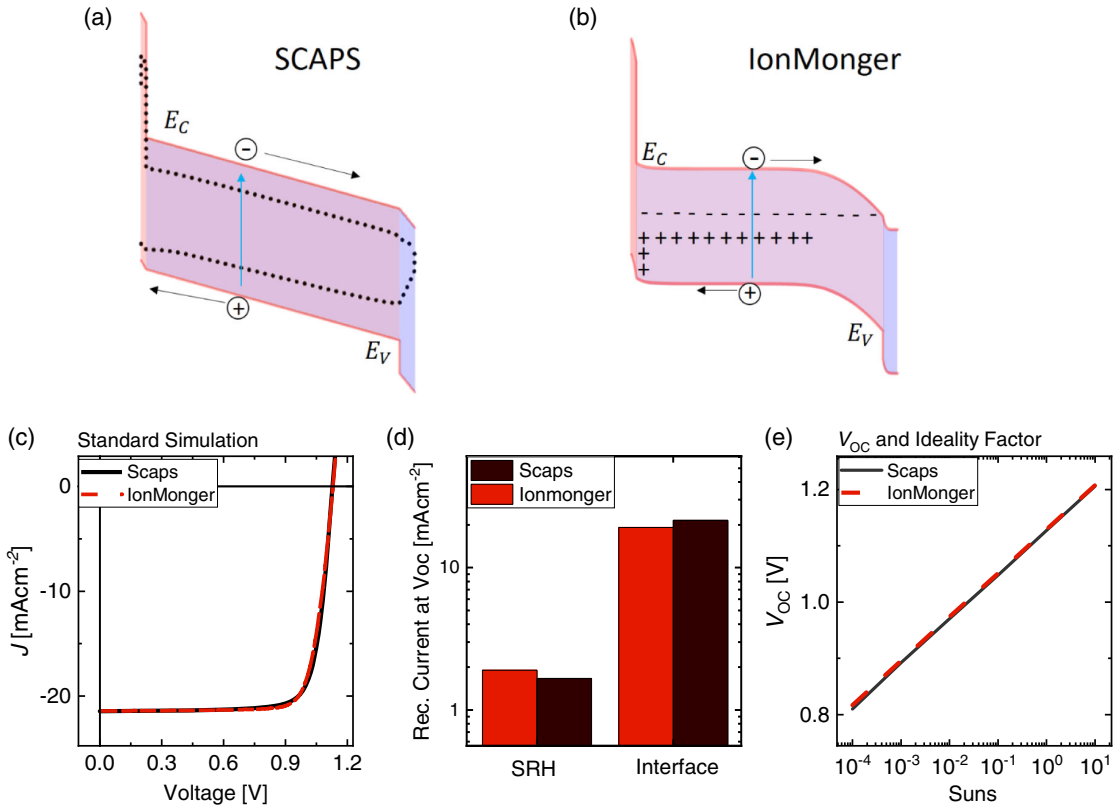

Figure 2. a,b) The band diagrams and resulting built-in potential obtained in SCAPS without mobile ions and IonMonger with mobile ions (6×10^{16} cm^{-3}) at short-circuit conditions. In case of IonMonger, the signs in the active layer denote the distribution of mobile halide vacancies ("+") and immobile remaining ions ("–"). c–e) A direct comparison of the *JV*, interfacial and bulk recombination currents, and the ideality factor for both programs. We note, for IonMonger a higher built-in voltage (100 mV) was assumed to compensate the ionic density.

simultaneously as well as both carrier types in the perovskite layer (Figure S9, Supporting Information). Only relatively small PCE improvements (≈1.5%) are possible by increasing the mobility in all the layers (**Figure 3**a). We note that this improvement comes likely from the hole mobility in the HTL because the PTAA layer mobility ($\mu_{PTAA} = 1.5 \times 10^{-4}$ cm^2 V^{-1} s^{-1}) with respect to the thickness of the layer ($d_{HTL} = 10$ nm) is significantly lower than the C_{60} and perovskite mobility ($\mu_{C60} = 1.0 \times 10^{-2}$ cm^2 V^{-1} s^{-1}, $\mu_{pero} = 1$ cm^2 V^{-1} s^{-1}) versus their thicknesses (30 and 500 nm, respectively). Therefore, PTAA sets the transport limitation despite the thin layer.

The situation is, however, markedly different upon chemical doping of the TLs. Figure 3b shows that both the FF and the V_{OC} improve significantly by increasing the donor/acceptor concentration in the TLs (from 10^{15} to 10^{20} cm^{-3}). This results in PCEs above 24% for the standard cell. We attribute this result to the effective increase of the built-in-field across the perovskite layer, which greatly reduces the minority-carrier concentration at the interfaces and thus interfacial recombination. This is because of two effects: 1) The potential drop across heavily doped TLs becomes negligible and 2) the energy offset of the doped TLs (difference between the ionization potential of the HTL and electron affinity of the ETL) maximizes the voltage drop across the perovskite (here 1.6 V). This is illustrated by the band diagrams in Figure 3c,d for an undoped (reference) cell at its V_{OC} as well as the same cell with doped TLs ($n_{dop} = 10^{19}$ cm^{-3}). The latter still exhibits a considerable internal field at the same applied voltage. Figure 3e shows that these concomitant effects lead to a significant reduction of the minority-carrier density at the interfaces, which suppresses the dominating interfacial recombination (see Figure S10a, Supporting Information) and increases the V_{OC} and the FF. Interestingly, the higher carrier density in the doped TL does not speed up the SRH recombination because the recombination rate is largely determined by the minority-carrier density at the interfaces. In general, the increase in the TL conductivity also reduces charge transport losses, although for our reference cell this effect is small due to the thin TLs and little transport losses (Figure 3a). The relative importance of these effects is further discussed in Figure S10b, Supporting Information. It is also interesting to note that both TLs need to be doped simultaneously as otherwise (if only one TL is doped) the other interface becomes the limiting component of the cell. Therefore, doping of the C_{60} layer allows considerable improvements until the PTAA/perovskite interface and the absorber layer itself are limiting the performance (Figure S11, Supporting Information). In contrast, almost no performance gains are achieved by doping the HTL only, as in this case the perovskite/C_{60} interface remains the limiting factor for the FF and V_{OC}. Finally, we emphasize that identical performance improvements can be achieved using only a thin doped

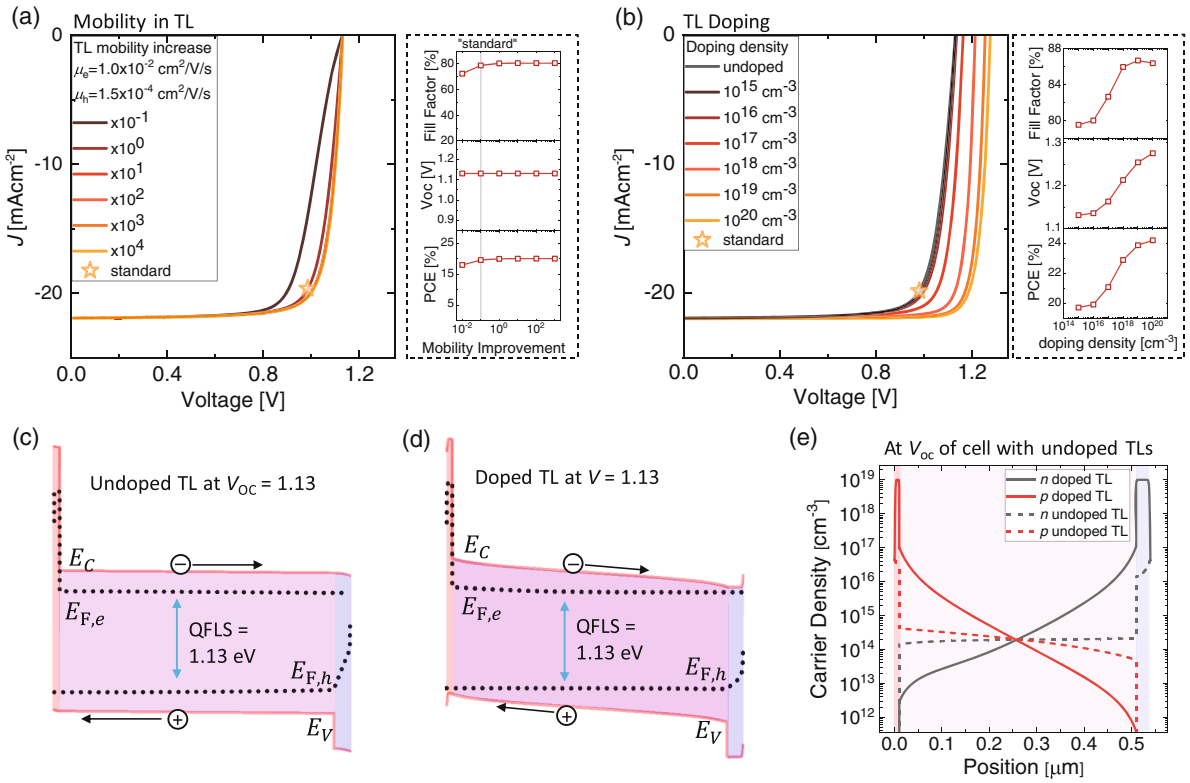

Figure 3. a) Numerically simulated current density versus voltage characteristics of p–i–n-type perovskite solar cells by simultaneously increasing the e^- and h^+ mobility (μ_{e^-}, μ_{h^+}) in the TLs by the specified factor in the legend, which allows relatively small efficiency improvements (<1%). b) By contrast, increasing the donor/acceptor doping density in the TLs (and keeping the mobility constant) can significantly increase the FF and V_{OC} of the cell. c,d) The resulting band diagrams of a cell with undoped and doped TLs (10^{19} cm^{-3}), respectively. Doping increases the effective driving field across the active layer, which repels minority carriers from the interfaces. e) The resulting carrier densities at the V_{OC} of the undoped, reference cell (1.13 V).

interlayer instead of a doped TL as shown in Figure S12, Supporting Information, which increases the experimental possibilities to reduce the critical interfacial recombination at the top interface through implementation of a doped interlayer.

2.3. Device Built-In Potential and Energy-Level Alignment

In a next step, we aimed to understand the impact of the built-in electrostatic potential difference (V_{BI}) and the energy-level alignment (E_{maj}) on cells with doped and undoped TLs. Both parameters have been shown to be critical for the device performance.[27,50–52,57,81] **Figure 4**a shows that a high built-in voltage above 1.2 V across the whole device is required in the undoped cell with a bandgap of 1.63 eV to efficiently extract the carriers and minimize FF losses and to prevent the formation of a reverse field in the device.[81] A similar picture appears to be the case for the cell with doped TLs ($n_{dop} = 10^{19}$ cm^{-3}), although the cell is more tolerant to a lower V_{BI} with >0.8 V being sufficient to avoid considerable PCE and FF losses. This is also shown in Figure S13, Supporting Information, for cells with and without doped TLs for different V_{BI} and E_{maj} values. In fact, we believe that in reality no metal work function mismatch may be required in case of strongly doped TLs, because carriers could tunnel through the TL to the electrode, which is challenging to implement numerically. Therefore, the observed PCE drop in Figure 4a at V_{BI} below 0.8 V may be incorrect. For the reference cell with undoped TLs, we find that V_{BI} below 1.0 V would not allow reproducing our high FFs of close to 80% even if the carrier mobilities are significantly increased (Figure S14, Supporting Information). Note that we assumed $V_{BI} = 1.2$ V in the standard settings, which is consistent with Mott–Schottky analysis in our cells. However, we acknowledge that we do not precisely know its origin considering the almost equal work function of ITO and Cu.[50] A large V_{BI} may indicate a considerable modification of the metal work functions in the presence of thin organic layers and/or the perovskite layer, or that the built-in potential is a result of remotely doped TL in our cell.[82,83]

Although a built-in potential across the complete device (in the dark) is indeed necessary to achieve a well-performing device, it is an interesting question whether it is possible that the V_{BI} drops only across the transport layers but not across the perovskite layer, as it is sometimes assumed in the literature. To investigate this, we artificially increase the dielectric constant in the perovskite layer which screens the field in the perovskite, thereby redistributing the relative potential drop across the perovskite layer and the TLs. Figure S15, Supporting Information, shows that when the mobilities in the TLs are kept constant, the efficiency decreases the larger the relative drop of the built-in voltage

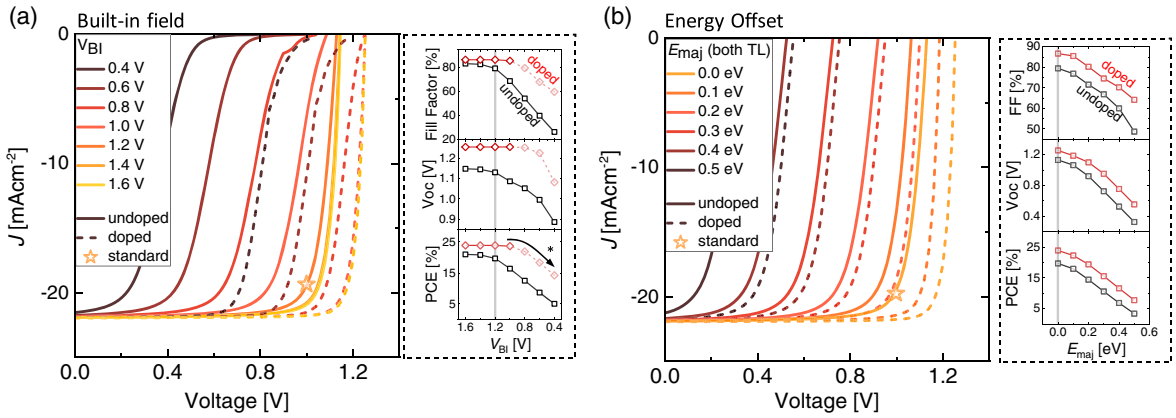

Figure 4. a) The impact of the device built-in potential (V_{BI}, here defined as the work function difference of the contact metals) and b) the energy alignment between the perovskite and the TLs on the *JV* characteristics and performance parameters of cells with doped and undoped TLs. In panel (b), the V_{BI} was kept constant (1.2 V). In the case of intrinsic TLs, increasing the V_{BI} from 1.2 V (standard cell) to 1.6 V allows us to improve the FF to 83.5%. Doped TLs are more tolerant with respect to the V_{BI}. Considerable losses appear below 1.0 V (marked with *); however, we attribute this to a limitation of the simulation model as discussed in the main text. In contrast, the energy-level mismatch between the perovskite and the TLs has a large impact on the device V_{OC} regardless of the doping of the TLs (and also in the presence of mobile ions).

across the transport layers, which reduces the voltage across the perovskite. This efficiency loss occurs even if the diffusion length in the perovskite layer (L_d) exceeds the film thickness (d) as observed experimentally.[84–86] The reason is that the charge extraction may not be limited by the perovskite layer but rather by the TLs, and also because interfacial recombination (which also impacts the FF) would be considerably enhanced if the V_{BI} was lower across the perovskite layer. Nevertheless, this does not mean that the potential cannot be partially flat across the perovskite active layer. For example, as shown in Figure 2b, in case of a significant mobile ion density, large field-free regions do exist in the perovskite layer; however, there is also a significant field at perovskite surfaces that repels minority carriers from the interface. This scenario considerably lowers the interfacial recombination, which means that the majority of the perovskite bulk could be field-free provided that the charge-carrier diffusion length in the perovskite is sufficient.

As to the impact of the energy-level alignment, Figure 4b shows that the energy levels of the transport layers need to be matched with respect to the energy levels of the perovskite layer and any downhill energetic offset for electrons (uphill for holes) would cause substantial V_{OC} and PCE losses regardless of whether the TLs are doped or not. Considering our previous study where we observed a match between the internal QFLS and the device V_{OC},[47] we expect that the alignment in our standard cells is well optimized. We note that any energetic offset will cause an equal loss in device V_{OC} as long as the interface between the perovskite and the misaligned TL is limiting the performance of the cell (and not another interface or the bulk).

2.4. Suppressed Recombination

Having analyzed the impact of the charge-carrier mobility, doping, mobile ions, and the energetics on the device performance, we now focus our attention on suppressing the defect recombination in the bulk of the material and at the interfaces.[87] In the following, we demonstrate the impact of S and τ_{bulk} as a function of the perovskite bandgap. **Figure 5**a shows the PCE of the standard cell as a function of the perovskite bandgap (red line). Interestingly, lowering the bandgap (from currently 1.63 eV to the optimum of ≈1.34 eV[5]) does not lead to significant performance gains (from 19.2% to 20.4%) due to the limitations imposed by the interfaces and the recombination in the bulk. We note that we kept the injection barriers between the contact metals and the TLs at 0.2 eV (as used in the standard simulations) and the energy levels of the transport layers well aligned as otherwise the PCE drops rapidly for higher and lower bandgaps (see Figure S16, Supporting Information). This also indicates difficulties in maintaining the perovskite performance when increasing the perovskite bandgap when the energy levels of the TLs do not move in accordance with the energetics of the perovskite absorber (Figure S17, Supporting Information). Although this may actually not be the limiting mechanism (considering a possible phase segregation; see Unger et al.[36]), it could be relevant when aiming for high-performance Si/perovskite tandem cells where a perovskite bandgap of 1.7 eV would be better than a typical gap of 1.6 eV.[88] Figure 5a also shows that switching off bulk recombination (blue) does not improve the PCE across the bandgap as it is the interface recombination that governs the PCE. Improvements up to a PCE of 23.8% are, however, possible if interface recombination is switched off completely (green), and close to 27% when both S and τ_{bulk} are switched off simultaneously (orange, "bimolecular only"). Considering now optimized yet already demonstrated recombination parameters, e.g., $S = 10\ \mathrm{cm\ s^{-1}}$[14,24,26] (at both interfaces) and $\tau_{bulk} = 10\ \mu\mathrm{s}$ (light blue),[18] allows reaching efficiencies of 25.3%, which is above the situation without interfacial recombination. Interestingly, the optimum bandgap in case of the optimized recombination parameters is considerably different (≈1.36–1.53 eV) than expected from the SQ model (1.12–1.4 eV). This is indicated by the dashed circles in Figure 5a.

In the following we tried to maximize the PCE using undoped TLs. First, we note that all simulations so far were performed

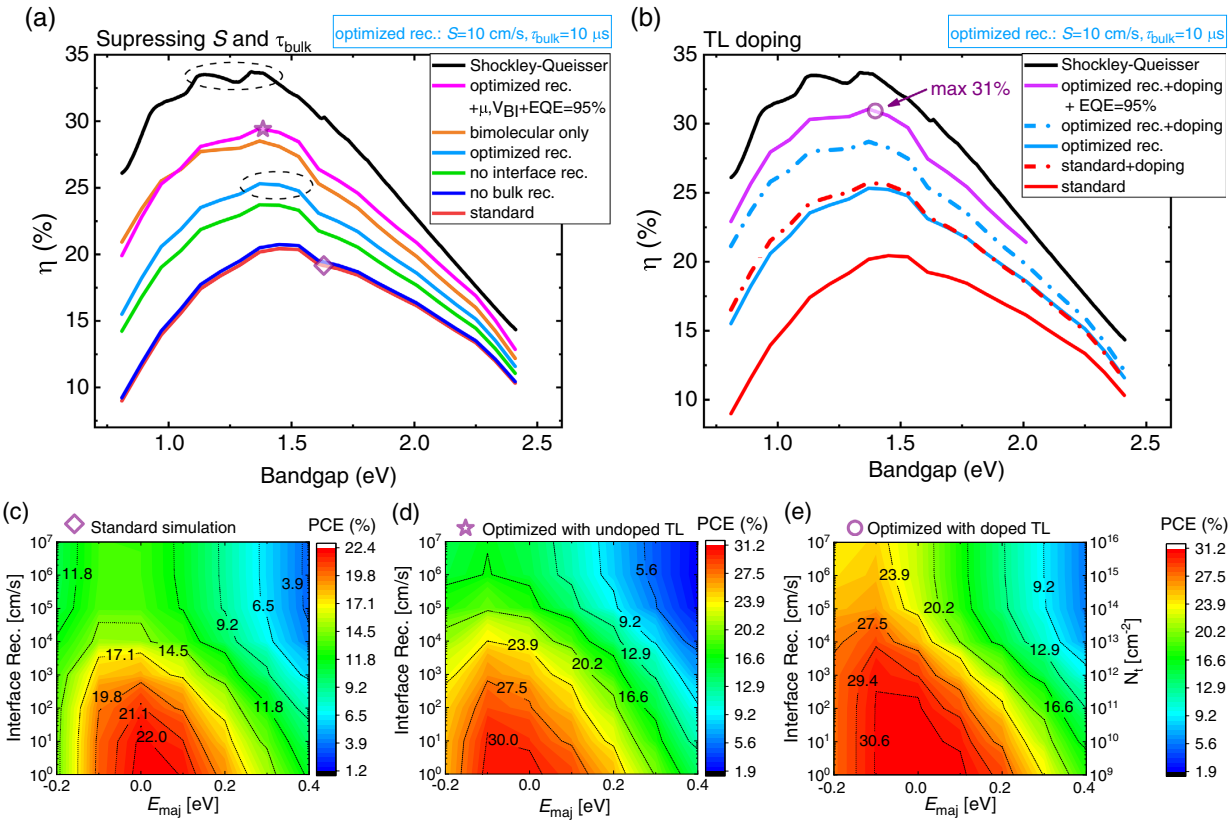

Figure 5. a) Numerically simulated PCE versus perovskite bandgap (E_{gap}) considering aligned perovskite/TL energy levels for different scenarios. Starting from the standard settings plotted in red ($S = 2000$ cm s^{-1} at the perovskite/ETL interface and bulk lifetime of 500 ns); (blue) in absence of bulk recombination; (green) in absence of interfacial recombination; (orange) in absence of interface and bulk recombination (bimolecular recombination only); (light blue) using optimized, yet plausible recombination parameters ($S = 10$ cm s^{-1} at both interfaces and a bulk-lifetime, τ_{bulk}, of 10 µs). The magenta curve shows an optimized cell with undoped TLs with optimized bulk and interface recombination, increased EQE (95% above gap), increased mobilities in all TLs by a factor of 10, and reduced injection barriers from the metal to the TLs (from 0.2 to 0.1 eV) resulting in a PCE of 29.4% at an optimum gap. b) The impact of TL doping (10^{19} cm^{-3}) for the standard cell in red (solid line without doping, dashed–dotted line with doping), the cell with optimized recombination parameters in light blue (solid line without doping, dashed–dotted line with doping), as well as for the cell with optimized recombination and light incoupling and EQE of 95% (solid magenta line). The black curve shows the PCE versus bandgap according to the Shockley–Queisser model.[5] c–e) PCE versus S and majority-carrier band offsets at both interfaces for the standard cell and the optimized cells with undoped and doped TLs, respectively. Note, a positive offset is defined as energy offset toward midgap (e.g. downhill for electrons), while a negative offset means an energy barrier for electrons and holes. In panel (e), the interfacial trap density is plotted on the right axis, which is proportional to S.

using an absorption model for a direct semiconductor that matches the experimentally measured absorption coefficient, α, and reproduces the short-circuit current in our standard cells with an average EQE slightly below 88% (Figure S1, Supporting Information). By further increasing the light incoupling and thus the EQE to 95% above the bandgap while simultaneously enhancing the carrier mobilities in all the layers by a factor of 10 and also reducing the injection barriers from the metals to the TLs from 0.2 to 0.1 eV (i.e., increasing the V_{BI}), we obtain a maximum efficiency of 29.4% at a bandgap of 1.36–1.4 eV. To check whether such high EQEs are reasonable in our devices, we also performed transfer-matrix simulations[89,90] (see Figure S18, Supporting Information, and corresponding discussion), which predict an average above-gap EQE slightly below 95% resulting in a J_{SC} that is ≈1 mA cm^{-2} lower than the current obtained with SCAPS for the best case, marked with an open star in Figure 5a. Nevertheless, we note that EQE spectra with an average EQE of ≈95% above the bandgap have been already demonstrated in efficient n–i–p-type devices with certified short-circuit currents and PCEs (23.48%).[91] This is clearly a key aspect to reach the 30% PCE milestone.

In the next step, starting from the simulation with optimized recombination parameters (light blue, max PCE = 25.3%), we further checked the impact of TL doping (using again 10^{19} cm^{-3} for both TLs). As shown in Figure 5b, this further enhanced the PCE to 28.7% (dashed–dotted light blue). As a comparison, the red lines show the corresponding PCE improvement versus E_{gap} upon TL doping in the standard cells. Finally, increasing the EQE to 95% results in a maximum PCE of 31% at a bandgap of 1.4 eV (purple line in Figure 5b). We note that for the same simulation parameters, the PCE stays above 30% for bandgaps of up to 1.5 eV, yet drops to 27.7% at a bandgap of 1.6 eV. We also checked under which conditions, in particular, for which energetic offsets and interface recombination

velocities, such high PCEs may be maintained. Figure 5c–e shows the PCE as a function of S and E_{maj} at both interfaces for our standard cells, as well as the optimized cells with undoped and doped TLs, respectively. Interestingly, Figure 5e shows that PCEs of ≈30% may be maintained in case of doped TLs even with interface recombination velocities of 1000 cm s^{-1} if the majority carrier band offsets are small (E_{maj} between −0.1 and 0 eV). However, higher values and positive energy offsets lead to rapid efficiency losses. We note that an analogous plot of PCE versus S and the bulk lifetime is shown in Figure S19, Supporting Information.

Based on the bandgap-dependent analysis in Figure 5, we propose two different cell architectures using doped and undoped TLs, which could be realized experimentally to reach the 30% PCE milestone. For the first cell shown in **Figure 6**a, we take advantage of the fact that doping allows increasing the TL thickness without compromising the device performance (Figure S20, Supporting Information, assuming that the parasitic absorption in the TL and the dopant is negligible).[42] This might be an important consideration from the manufacturing perspective as it could help to protect the perovskite from moisture and oxygen ingress. Here, we assumed a bandgap of 3.5 eV for the bottom TL, which is comparable to the bandgaps of TiO_2 (3.3 eV), SnO_2 (3.6 eV), and NiO_x.[92,93] Using 100 nm thick TLs, realistic interface recombination velocities of 10 cm s^{-1},[14,24,26] bulk lifetimes of 10 µs (shown in deQuilettes et al.[18]), and doped TLs ($n_{dop} = 10^{19}$ cm^{-3}),[43] we can simulate a PCE of 30% even for a bandgap of 1.5 eV (which is within reach for FAPI-based perovskites).[34] However, it is clear that realizing a stable doping experimentally without critically enhancing S, which may in

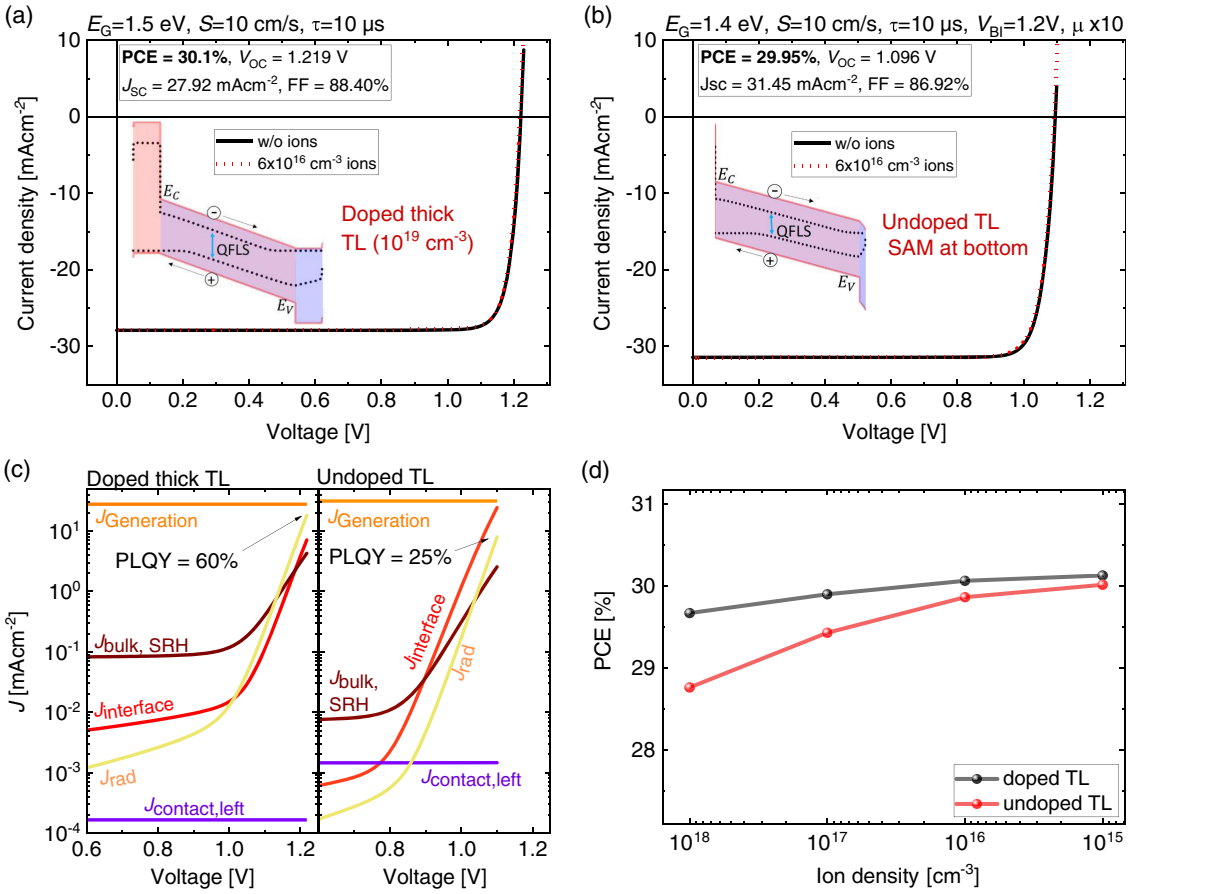

Figure 6. a) Numerically simulated current density versus voltage (JV) characteristics of p–i–n-type cells with comparatively thick, doped TLs (10^{19} cm^{-3}) and a bandgap of 1.5 eV, interface recombination velocities (S) of 10 cm s^{-1}, a bulk lifetime of 10 µs, and a PCE of ≈30%. As shown in this study, the doped TLs maximize the field across the perovskite, which enhances the PCE despite the significant S values. b) Numerically simulated JV characteristics of a perovskite cell with a 1 nm thick self-assembled monolayer at the bottom as an alternative strategy to reach 30% with undoped TLs. Note that the short-circuit current and the open-circuit voltage differ between the two cells due to their different bandgaps. The red dotted lines in panel (a) and (b) demonstrate that adding the measured ion density of ≈6 × 10^{16} cm^{-3} while keeping the other simulation parameters identical has an almost negligible effect on the steady-state performance in these two high-efficiency systems. c) The parallel recombination currents as a function of applied voltage in both cells w/o ions. The graph also demonstrates a PLQY of ≈60% for the cell with doped TLs and ≈25% for the SAM-based cell under open-circuit conditions. This difference is because the built-in potential drop across the 20 nm thick top TL renders the cell with undoped TLs more vulnerable to interfacial recombination. Therefore, when aiming to avoid doping and keeping the S at a realistic value ($S > 1$ cm s^{-1}), such high PCEs can only be reached in case of ultrathin TLs such as SAMs. d) The steady-state efficiency of the doped-TL cells versus ion density reveals a small efficiency loss for ion densities of up to 1 × 10^{18} cm^{-3}.

reality overcompensate for the potential benefits (Figure 5e), will remain a critical experimental challenge. We note that in principle, a thin insulating layer could be implemented to avoid a direct contact between the doped TL and the perovskite, potentially lowering the interfacial recombination (Figure S21, Supporting Information). The second cell shown in Figure 6b is based on a 1 nm thick self-assembled monolayer as bottom TL. It was recently shown[94–96] that a self-assembled monolayer (SAM) can replace and even outperform the omnipresent PTAA layer in p–i–n-type cells with negligible recombination at the bottom interface. Using a SAM at the bottom and a thin TL at the top (20 nm) and the same setting as discussed earlier for the optimized cell in Figure 4a also allows us to reach the 30% milestone; however, we emphasize that this is strictly limited by the thickness of the layer. For example, implementing two 100 nm thick TLs for this particular device reduces the PCE to 27%, which is due to the increased interface loss when lowering the V_{BI} across the perovskite. Nevertheless, we note that the SAM is likely beneficial in terms of parasitic absorption compared to doped TLs and in terms of device stability.[96] The parallel recombination currents in the device for both cells based on the doped TL and the SAM are shown in Figure 6c. Finally, by implementing the earlier quantified ion density ($n_{ion} \approx 6 \times 10^{16}\,cm^{-3}$), we observed that the steady-state performance of both proposed high-efficiency cells is hardly affected by the mobile ion density (red dotted lines in Figure 6a,b). In fact, Figure 6d shows that this holds true for ion densities of up to up to $1 \times 10^{18}\,cm^{-3}$. This finding can be explained by the increased V_{BI} and reduced S, which mitigates the effect of the ion density as previously observed.[70] Therefore, we can conclude that although mobile ions are a key for current state-of-the-art perovskite devices and their stability, they do not represent a significant roadblock for perovskite solar cells reaching the 30% efficiency milestone.

3. Conclusion

In summary, in this work we explored possible optimization strategies to advance the PCEs of perovskite solar cells beyond those of monocrystalline silicon (>26%) and GaAs cells (>29%). To this end, we established a standard simulation to describe our reference (standard) p–i–n-type cells with an efficiency of close to 20% using SCAPS and IonMonger to incorporate mobile ions. We then checked a wide range of simulation parameters and discussed the importance of μ, n_{ion}, n_{dop}, V_{BI}, E_{maj}, E_{gap}, S, and τ_{bulk} as key parameters in defining the cells' performance. In combination with transient capacitance measurements and charge extraction, we demonstrated that the ion density is rather significant ($\geq 6 \times 10^{16}\,cm^{-3}$), which significantly redistributes the internal field. Starting from the standard cells, we showed that (tenfold) optimization of the mobilities of the TL and the perovskite layer will result in comparatively marginal PCE improvements (≈1% absolute). Instead, doping the TLs relaxes the need of electrodes with large work function offsets and enables drastic FF and V_{OC} gains. We attributed this result to an effective increase in the V_{BI} across the perovskite layer, which drives minority carriers away from the interfaces. We further discussed the need of a high built-in field across all stack layers, including the absorber layer, where a field is required at the surfaces. Also, energy-level matching between the perovskite and the TL remains a necessity to avoid PCE losses irrespective of the TL doping and the presence of mobile ions. We then varied the perovskite bandgap for cells with suppressed defect recombination in the bulk and/or the interface. In combination with doped TLs, we identified that recombination parameters that have already been demonstrated in the recent literature ($\tau_{bulk} = 10\,\mu s$ and $S = 10\,cm\,s^{-1}$) would allow PCEs of up to 31% for a perovskite with a bandgap of 1.4 eV if an average above-gap EQE of 95% can be realized. Based on these findings, we numerically demonstrated the feasibility of 30% efficient perovskite cells with comparatively thick (≈100 nm), doped TLs ($\approx 10^{19}\,cm^{-3}$) or thin doped interlayers by implementing a perovskite layer with realistic interface recombination velocities ($S = 10\,cm\,s^{-1}$) and a bandgap of 1.5 eV. Alternatively, cells with ultrathin TLs (e.g., by implementing self-assembled monolayers at the bottom contact) may also allow us to reach the 30% milestone if the V_{BI} across the perovskite layer can be maximized to supress the critical interface recombination. However, although doped TLs allow us to relax several strict requirements to realize such near-ideal solar cells, e.g., by allowing us to use thicker TLs and by increasing the tolerance against interfacial defects, SAMs are beneficial in terms of optical losses and device stability, which is a key for future developments. Finally, we also demonstrated that the rather high ion density does not represent a major roadblock to unlock efficiencies at the radiative limits and therefore, we expect that perovskite solar cells will become the most efficient single-junction solar technology in the near future.

Supporting Information

Supporting Information is available from the Wiley Online Library or from the author.

Acknowledgements

This work was funded by the Deutsche Forschungsgemeinschaft (DFG, German Research Foundation) project numbers 423749265 and 424216076 as well as by HyPerCells (a joint graduate school of the Potsdam University and the HZB). The work of M.H.F. and B.E. is part of the Dutch Research Council (NWO) and was performed at the research institute AMOLF. The work by V.M.L.C. is supported by a grant from STW/NWO (VIDI 13476). This is a publication by the FOM Focus Group "Next Generation Organic Photovoltaics," participating in the Dutch Institute for Fundamental Energy Research (DIFFER). T.K. acknowledges the Helmholtz Association for funding via the PEROSEED project. The authors also thank Nicola Courtier for her kind support with IonMonger.

Open access funding enabled and organized by Projekt DEAL.

Conflict of Interest

The authors declare no conflict of interest.

Author Contributions

J.D. performed most of the simulations, including the IonMonger simulations, and analyzed all the simulation results and contributed to manuscript drafting. P.C. contributed to numerical simulations, electrical and PL measurements, device fabrication, and data interpretation. M.H.F performed transient capacitance measurements and analyzed the impact

of mobile ions. V.M.L.C. contributed to mobile ion simulations and corresponding data analysis. S.R. performed transient capacitance measurements and analyzed corresponding data. F.J. contributed to hysteresis measurements. M.A. performed experiments with doped transport layers and analysed results related to doping. L.P.T. performed BACE measurements and corresponding data analysis. E.G.-P. contributed to solar cell fabrication. F.P-C. contributed to the BACE measurements and corresponding data analysis. C.D. supervised the transient capacitance measurements and contributed to the analysis of mobile ions. B.E. supervised the transient capacitance measurements and contributed to the analysis of mobile ions. T.U. established the SCAPS simulations, performed numerical simulations, and analyzed the simulation results. T.K. performed numerical simulations, interpreted the data, and contributed to manuscript drafting. D.N. supervised the study, contributed to manuscript drafting and interpretation of all data. M.S. planned the project, drafted the manuscript, fabricated cells, and performed electrical and PL measurements, numerical simulations, and analyzed all the data. All authors proofread the manuscript.

Data Availability Statement

The data that support the findings of this study are available from the corresponding author upon reasonable request.

Keywords

perovskite solar cells, solar cell hysteresis, solar cell simulations, transport-layer doping

Received: March 25, 2021
Revised: May 26, 2021
Published online:

[1] NREL, *Best Research-Cell Efficiencies*, NREL, Golden, CO **2020**.
[2] K. Yamamoto, K. Yoshikawa, H. Uzu, D. Adachi, *Jpn. J. Appl. Phys.* **2018**, *57*, 08RB20.
[3] K. Yoshikawa, H. Kawasaki, W. Yoshida, T. Irie, K. Konishi, K. Nakano, T. Uto, D. Adachi, M. Kanematsu, H. Uzu, K. Yamamoto, *Nat. Energy* **2017**, *2*, 17032.
[4] W. Shockley, H. J. Queisser, *J. Appl. Phys.* **1961**, *32*, 510.
[5] S. Rühle, *Sol. Energy* **2016**, *130*, 139.
[6] O. D. Miller, E. Yablonovitch, S. R. Kurtz, *IEEE J. Photovoltaics* **2012**, *2*, 303.
[7] D. Bryant, N. Aristidou, S. Pont, I. Sanchez-Molina, T. Chotchunangatchaval, S. Wheeler, J. R. Durrant, S. A. Haque, *Energy Environ. Sci.* **2016**, *9*, 1655.
[8] G. Divitini, S. Cacovich, F. Matteocci, L. Cinà, A. Di Carlo, C. Ducati, *Nat. Energy* **2016**, *1*, 15012.
[9] Q. Wang, B. Chen, Y. Liu, Y. Deng, Y. Bai, Q. Dong, J. Huang, *Energy Environ. Sci.* **2017**, *10*, 516.
[10] P. Billen, E. Leccisi, S. Dastidar, S. Li, L. Lobaton, S. Spatari, A. T. Fafarman, V. M. Fthenakis, J. B. Baxter, *Energy* **2019**, *166*, 1089.
[11] S. Hong, J. Lee, H. Kang, G. Kim, S. Kee, J. H. Lee, S. Jung, B. Park, S. Kim, H. Back, K. Yu, K. Lee, *Sci. Adv.* **2018**, *4*, eaat3604.
[12] M. Abdi-Jalebi, Z. Andaji-Garmaroudi, S. Cacovich, C. Stavrakas, B. Philippe, J. M. Richter, M. Alsari, E. P. Booker, E. M. Hutter, A. J. Pearson, S. Lilliu, T. J. Savenije, H. Rensmo, G. Divitini, C. Ducati, R. H. Friend, S. D. Stranks, *Nature* **2018**, *555*, 497.
[13] I. L. Braly, D. W. DeQuilettes, L. M. Pazos-Outón, S. Burke, M. E. Ziffer, D. S. Ginger, H. W. Hillhouse, *Nat. Photonics* **2018**, *12*, 355.
[14] Z. Liu, L. Krückemeier, B. Krogmeier, B. Klingebiel, J. A. Márquez, S. Levcenko, S. Öz, S. Mathur, U. Rau, T. Unold, T. Kirchartz, *ACS Energy Lett.* **2019**, *4*, 110.
[15] Q. Jiang, Y. Zhao, X. Zhang, X. Yang, Y. Chen, Z. Chu, Q. Ye, X. Li, Z. Yin, J. You, *Nat. Photonics* **2019**, *13*, 460.
[16] Y. Cao, N. Wang, H. Tian, J. Guo, Y. Wei, H. Chen, Y. Miao, W. Zou, K. Pan, Y. He, H. Cao, Y. Ke, M. Xu, Y. Wang, M. Yang, K. Du, Z. Fu, D. Kong, D. Dai, Y. Jin, G. Li, H. Li, Q. Peng, J. Wang, W. Huang, *Nature* **2018**, *562*, 249.
[17] M. Stolterfoht, M. Grischek, P. Caprioglio, C. M. Wolff, E. Gutierrez-Partida, F. Peña-Camargo, D. Rothhardt, S. Zhang, M. Raoufi, J. Wolansky, M. Abdi-Jalebi, S. D. Stranks, S. Albrecht, T. Kirchartz, D. Neher, *Adv. Mater.* **2020**, *32*, 2000080.
[18] D. W. deQuilettes, S. Koch, S. Burke, R. K. Paranji, A. J. Shropshire, M. E. Ziffer, D. S. Ginger, *ACS Energy Lett.* **2016**, *1*, 438.
[19] I. L. Braly, H. W. Hillhouse, *J. Phys. Chem. C* **2016**, *120*, 893.
[20] V. Sarritzu, N. Sestu, D. Marongiu, X. Chang, S. Masi, A. Rizzo, S. Colella, F. Quochi, M. Saba, A. Mura, G. Bongiovanni, *Sci. Rep.* **2017**, *7*, 44629.
[21] N. Wu, Y. Wu, D. Walter, H. Shen, T. Duong, D. Grant, C. Barugkin, X. Fu, J. Peng, T. White, K. Catchpole, K. Weber, *Energy Technol.* **2017**, *5*, 1827.
[22] M. Stolterfoht, C. M. Wolff, J. A. Márquez, S. Zhang, C. J. Hages, D. Rothhardt, S. Albrecht, P. L. Burn, P. Meredith, T. Unold, D. Neher, *Nat. Energy* **2018**, *3*, 847.
[23] B. Krogmeier, F. Staub, D. Grabowski, U. Rau, T. Kirchartz, *Sustain. Energy Fuels* **2018**, *2*, 1027.
[24] J. Wang, W. Fu, S. Jariwala, I. Sinha, A. K. Y. Jen, D. S. Ginger, *ACS Energy Lett.* **2019**, *4*, 222.
[25] S. Olthof, K. Meerholz, *Sci. Rep.* **2017**, *7*, 40267.
[26] F. Staub, H. Hempel, J. C. Hebig, J. Mock, U. W. Paetzold, U. Rau, T. Unold, T. Kirchartz, *Phys. Rev. Appl.* **2016**, *6*, 044017.
[27] C. M. Wolff, F. Zu, A. Paulke, L. P. Toro, N. Koch, D. Neher, *Adv. Mater.* **2017**, *29*, 1700159.
[28] E. M. Hutter, J. J. Hofman, M. L. Petrus, M. Moes, R. D. Abellón, P. Docampo, T. J. Savenije, *Adv. Energy Mater.* **2017**, *7*, 1602349.
[29] C. J. Hages, A. Redinger, S. Levcenko, H. Hempel, M. J. Koeper, R. Agrawal, D. Greiner, C. A. Kaufmann, T. Unold, *Adv. Energy Mater.* **2017**, *7*, 1700167.
[30] A. Kojima, K. Teshima, Y. Shirai, T. Miyasaka, *J. Am. Chem. Soc.* **2009**, *131*, 6050.
[31] S. S. Shin, E. J. Yeom, W. S. Yang, S. Hur, M. G. Kim, J. Im, J. Seo, J. H. Noh, S. Il Seok, *Science* **2017**, *356*, 167.
[32] T. Liu, Y. Zong, Y. Zhou, M. Yang, Z. Li, O. S. Game, K. Zhu, R. Zhu, Q. Gong, N. P. Padture, *Chem. Mater.* **2017**, *29*, 3246.
[33] Y. Yu, C. Wang, C. R. Grice, N. Shrestha, J. Chen, D. Zhao, W. Liao, A. J. Cimaroli, P. J. Roland, R. J. Ellingson, Y. Yan, *ChemSusChem* **2016**, *9*, 3288.
[34] W. S. Yang, J. H. Noh, N. J. Jeon, Y. C. Kim, S. Ryu, J. Seo, S. Il Seok, *Science* **2015**, *348*, 1234.
[35] H. Min, M. Kim, S. U. Lee, H. Kim, G. Kim, K. Choi, J. H. Lee, S. I. Seok, *Science (80-.)*. **2019**, *366*, 749.
[36] E. L. Unger, L. Kegelmann, K. Suchan, D. Sörell, L. Korte, S. Albrecht, *J. Mater. Chem. A* **2017**, *5*, 11401.
[37] S. A. L. Weber, I. M. Hermes, S. H. Turren-Cruz, C. Gort, V. W. Bergmann, L. Gilson, A. Hagfeldt, M. Graetzel, W. Tress, R. Berger, *Energy Environ. Sci.* **2018**, *11*, 2404.
[38] J. Kromdijk, K. Głowacka, L. Leonelli, S. T. Gabilly, M. Iwai, K. K. Niyogi, S. P. Long, *Science* **2016**, *354*, 857.
[39] B. Zhao, M. Abdi-Jalebi, M. Tabachnyk, H. Glass, V. S. Kamboj, W. Nie, A. J. Pearson, Y. Puttisong, K. C. Gödel, H. E. Beere, D. A. Ritchie, A. D. Mohite, S. E. Dutton, R. H. Friend, A. Sadhanala, *Adv. Mater.* **2017**, *29*, 1604744.

[40] Y. Ogomi, A. Morita, S. Tsukamoto, T. Saitho, N. Fujikawa, Q. Shen, T. Toyoda, K. Yoshino, S. S. Pandey, T. Ma, S. Hayase, *J. Phys. Chem. Lett.* **2014**, *5*, 1004.
[41] R. Lin, K. Xiao, Z. Qin, Q. Han, C. Zhang, M. Wei, M. I. Saidaminov, Y. Gao, J. Xu, M. Xiao, A. Li, J. Zhu, E. H. Sargent, H. Tan, *Nat. Energy* **2019**, *4*, 864.
[42] C. Momblona, L. Gil-Escrig, E. Bandiello, E. M. Hutter, M. Sessolo, K. Lederer, J. Blochwitz-Nimoth, H. J. Bolink, *Energy Environ. Sci.* **2016**, *9*, 3456.
[43] S. Olthof, S. Mehraeen, S. K. Mohapatra, S. Barlow, V. Coropceanu, J. L. Brédas, S. R. Marder, A. Kahn, *Phys. Rev. Lett.* **2012**, *109*, 176601.
[44] Q. Wang, C. Bi, J. Huang, *Nano Energy* **2015**, *15*, 275.
[45] M. Stolterfoht, C. M. Wolff, Y. Amir, A. Paulke, L. Perdigón-Toro, P. Caprioglio, D. Neher, *Energy Environ. Sci.* **2017**, *10*, 1530.
[46] G. Richardson, S. E. J. O'Kane, R. G. Niemann, T. A. Peltola, J. M. Foster, P. J. Cameron, A. B. Walker, *Energy Environ. Sci.* **2016**, *9*, 1476.
[47] P. Calado, A. M. Telford, D. Bryant, X. Li, J. Nelson, B. C. O'Regan, P. R. F. Barnes, *Nat. Commun.* **2016**, *7*, 13831.
[48] M. H. Futscher, J. M. Lee, L. McGovern, L. A. Muscarella, T. Wang, M. A. HaiderFakharuddin, A. IFakharuddin, L. Schmidt-Mende, B. Ehrler, *Mater. Horizons* **2019**, *6*, 1497.
[49] N. Tessler, Y. Vaynzof, *ACS Energy Lett.* **2020**, *5*, 1260.
[50] M. Stolterfoht, P. Caprioglio, C. M. Wolff, J. A. Márquez, J. Nordmann, S. Zhang, D. Rothhardt, U. Hörmann, Y. Amir, A. Redinger, L. Kegelmann, F. Zu, S. Albrecht, N. Koch, T. Kirchartz, M. Saliba, T. Unold, D. Neher, *Energy Environ. Sci.* **2019**, *12*, 2778.
[51] T. Kirchartz, *Philos. Trans. R. Soc. A Math. Phys. Eng. Sci.* **2019**, *377*, 20180286.
[52] M. Zhang, Q. Chen, R. Xue, Y. Zhan, C. Wang, J. Lai, J. Yang, H. Lin, J. Yao, Y. Li, L. Chen, Y. Li, *Nat. Commun.* **2019**, *10*, 4593.
[53] S. Reichert, J. Flemming, Q. An, Y. Vaynzof, J.-F. Pietschmann, C. Deibel, *Phys. Rev. Appl.* **2020**, *13*, 034018.
[54] L. Bertoluzzi, C. C. Boyd, N. Rolston, J. Xu, R. Prasanna, B. C. O'Regan, M. D. McGehee, *Joule* **2020**, *4*, 109.
[55] A. Walsh, D. O. Scanlon, S. Chen, X. G. Gong, S. H. Wei, *Angew. Chem., Int. Ed.* **2015**, *54*, 1791.
[56] R. A. Belisle, P. Jain, R. Prasanna, T. Leijtens, M. D. McGehee, *ACS Energy Lett.* **2016**, *1*, 556.
[57] P. Schulz, E. Edri, S. Kirmayer, G. Hodes, D. Cahen, A. Kahn, *Energy Environ. Sci.* **2014**, *7*, 1377.
[58] L. E. Polander, P. Pahner, M. Schwarze, M. Saalfrank, C. Koerner, K. Leo, *APL Mater.* **2014**, *2*, 081503.
[59] I. Gelmetti, N. F. Montcada, A. Pérez-Rodríguez, E. Barrena, C. Ocal, I. García-Benito, A. Molina-Ontoria, N. Martín, A. Vidal-Ferran, E. Palomares, *Energy Environ. Sci.* **2019**, *12*, 1309.
[60] M. Cai, N. Ishida, X. Li, X. Yang, T. Noda, Y. Wu, F. Xie, H. Naito, D. Fujita, L. Han, *Joule* **2018**, *2*, 296.
[61] I. M. Hermes, Y. Hou, V. W. Bergmann, C. J. Brabec, S. A. L. Weber, *J. Phys. Chem. Lett.* **2018**, *9*, 6249.
[62] J. Byeon, J. Kim, J.-Y. Kim, G. Lee, K. Bang, N. Ahn, M. Choi, *ACS Energy Lett.* **2020**, *5*, 2580.
[63] J.-P. Correa-Baena, W. Tress, K. Domanski, E. H. Anaraki, S.-H. Turren-Cruz, B. Roose, P. P. Boix, M. Grätzel, M. Saliba, A. Abate, A. Hagfeldt, *Energy Environ. Sci.* **2017**, *10*, 1207.
[64] S. Pisoni, M. Stolterfoht, J. Löckinger, T. Moser, Y. Jiang, P. Caprioglio, D. Neher, S. Buecheler, A. N. Tiwari, *Sci. Technol. Adv. Mater.* **2019**, *20*, 786.
[65] T. Du, W. Xu, M. Daboczi, J. Kim, S. Xu, C. T. Lin, H. Kang, K. Lee, M. J. Heeney, J. S. Kim, J. R. Durrant, M. A. McLachlan, *J. Mater. Chem. A* **2019**, *7*, 18971.
[66] J. G. Fossum, *IEEE Trans. Electron Devices* **1977**, *24*, 322.
[67] M. Burgelman, P. Nollet, S. Degrave, *Thin Solid Films* **2000**, *361*, 527.
[68] K. Decock, P. Zabierowski, M. Burgelman, *J. Appl. Phys.* **2012**, *111*, 043703.
[69] N. E. Courtier, J. M. Cave, A. B. Walker, G. Richardson, J. M. Foster, *J. Comput. Electron.* **2019**, *18*, 1435.
[70] N. E. Courtier, J. M. Cave, J. M. Foster, A. B. Walker, G. Richardson, *Energy Environ. Sci.* **2019**, *12*, 396.
[71] X. Zheng, B. Chen, J. Dai, Y. Fang, Y. Bai, Y. Lin, H. Wei, X. C. Zeng, J. Huang, *Nat. Energy* **2017**, *2*, 17102.
[72] J. M. Richter, M. Abdi-Jalebi, A. Sadhanala, M. Tabachnyk, J. P. H. Rivett, L. M. Pazos-Outón, K. C. Gödel, M. Price, F. Deschler, R. H. Friend, *Nat. Commun.* **2016**, *7*, 13941.
[73] T. S. Sherkar, C. Momblona, L. Gil-Escrig, H. J. Bolink, L. J. A. Koster, *Adv. Energy Mater.* **2017**, *7*, 1602432.
[74] L. M. Pazos-Outon, M. Szumilo, R. Lamboll, J. M. Richter, M. Crespo-Quesada, M. Abdi-Jalebi, H. J. Beeson, M. Vruini, M. Alsari, H. J. Snaith, B. Ehrler, R. H. Friend, F. Deschler, *Science* **2016**, *351*, 1430.
[75] L. M. Pazos-Outón, T. P. Xiao, E. Yablonovitch, *J. Phys. Chem. Lett.* **2018**, *9*, 1703.
[76] T. Kirchartz, F. Staub, U. Rau, *ACS Energy Lett.* **2016**, *1*, 731.
[77] R. Brenes, M. Laitz, J. Jean, D. W. DeQuilettes, V. Bulović, *Phys. Rev. Appl.* **2019**, *12*, 014017.
[78] P. Caprioglio, M. Stolterfoht, C. M. Wolff, T. Unold, B. Rech, S. Albrecht, D. Neher, *Adv. Energy Mater.* **2019**, *9*, 1901631.
[79] V. M. Le Corre, M. Stolterfoht, L. Perdigón Toro, M. Feuerstein, C. Wolff, L. Gil-Escrig, H. J. Bolink, D. Neher, L. J. A. Koster, *ACS Appl. Energy Mater.* **2019**, *2*, 6280.
[80] M. H. Futscher, M. K. Gangishetty, D. N. Congreve, B. Ehrler, *J. Chem. Phys.* **2020**, *152*, 044202.
[81] O. J. Sandberg, J. Kurpiers, M. Stolterfoht, D. Neher, P. Meredith, S. Shoaee, A. Armin, *Adv. Mater. Interfaces* **2020**, *7*, 2000041.
[82] U. Würfel, *Adv. Energy Mater.* **2016**, *6*, 1600594.
[83] F. A. Nüesch, *Chim. Int. J. Chem.* **2013**, *67*, 796.
[84] C. Wehrenfennig, G. E. Eperon, M. B. Johnston, H. J. Snaith, L. M. Herz, *Adv. Mater.* **2014**, *26*, 1584.
[85] M. B. Johnston, L. M. Herz, *Acc. Chem. Res.* **2016**, *49*, 146.
[86] S. D. Stranks, G. E. Eperon, G. Grancini, C. Menelaou, M. J. P. Alcocer, T. Leijtens, L. M. Herz, A. Petrozza, H. J Snaith, *Science* **2013**, *342*, 341.
[87] T. S. Sherkar, C. Momblona, L. Gil-Escrig, J. Ávila, M. Sessolo, H. J. Bolink, L. J. A. Koster, *ACS Energy Lett.* **2017**, *2*, 1214.
[88] F. Sahli, J. Werner, B. A. Kamino, M. Bräuninger, R. Monnard, B. Paviet-Salomon, L. Barraud, L. Ding, J. J. Diaz Leon, D. Sacchetto, G. Cattaneo, M. Despeisse, M. Boccard, S. Nicolay, Q. Jeangros, B. Niesen, C. Ballif, *Nat. Mater.* **2018**, *17*, 820.
[89] P. Peumans, A. Yakimov, S. R. Forrest, *J. Appl. Phys.* **2003**, *93*, 3693.
[90] L. A. A. Pettersson, L. S. Roman, O. Inganaìŝ, *J. Appl. Phys.* **1999**, *86*, 487.
[91] M. Kim, G.-H. Kim, T. K. Lee, I. W. Choi, H. W. Choi, Y. Jo, Y. J. Yoon, J. W. Kim, J. Lee, D. Huh, H. Lee, S. K. Kwak, J. Y. Kim, D. S. Kim, *Joule* **2019**, *3*, 2179.
[92] L. Kegelmann, C. M. Wolff, C. Awino, F. Lang, E. L. Unger, L. Korte, T. Dittrich, D. Neher, B. Rech, S. Albrecht, *ACS Appl. Mater. Interfaces* **2017**, *9*, 17245.
[93] S. Pang, C. Zhang, H. Dong, D. Chen, W. Zhu, H. Xi, J. Chang, Z. Lin, J. Zhang, Y. Hao, *ACS Appl. Energy Mater.* **2019**, *2*, 4700.
[94] A. Magomedov, A. Al-Ashouri, E. Kasparavičius, S. Strazdaite, G. Niaura, M. Jošt, T. Malinauskas, S. Albrecht, V. Getautis, *Adv. Energy Mater.* **2018**, *8*, 1801892.
[95] A. Al-Ashouri, A. Magomedov, M. Roß, M. Jošt, M. Talaikis, G. Chistiakova, T. Bertram, J. A Márquez, E. Köhnen,

E. Kasparavičius, S. Levcenco, L. Gil-Escrig, C. J. Hages, R. Schlatmann, B. Rech, T. Malinauskas, T. Unold, C. A. Kaufmann, L. Korte, G. Niaura, V. Getautis, S. Albrecht, *Energy Environ. Sci.* **2019**, *12*, 3356.

[96] A. Al-Ashouri, E. Köhnen, B. Li, A. Magomedov, H. Hempel, P. Caprioglio, J. A. Márquez, A. B. Morales Vilches, E. Kasparavicius, J. A. Smith, N. Phung, D. Menzel, M. Grischek, L. Kegelmann, D. Skroblin, C. Gollwitzer, T. Malinauskas, M. Jošt, G. Matič, B. Rech, R. Schlatmann, M. Topič, L. Korte, A. Abate, B. Stannowski, D. Neher, M. Stolterfoht, T. Unold, V. Getautis, S. Albrecht, *Science* **2020**, *370*, 1300.